DRAFT VERSION SEPTEMBER 2, 2016
Preprint typeset using LaTeX style AASTeX6 v. 1.0

arXiv:1509.08115v2 [astro-ph.HE] 31 Aug 2016

NUSTAR OBSERVATIONS OF MAGNETAR 1E 1048.1−5937

C. YANG[1,2], R. F. ARCHIBALD[2], J. K. VOGEL[3], H. AN[4], V. M. KASPI[2], S. GUILLOT[5], A. M. BELOBORODOV[6], M. PIVOVAROFF[3]

[1]Beijing Institute of Technology, 5 South Zhongguancun Street,Haidian District, Beijing 100081,China
[2]Department of Physics & McGill Space Institute, McGill University, 3600 University St., Montreal, QC, H3A 2T8, Canada
[3]Lawrence Livermore National Laboratory, PLS/Physics, Livermore, CA 94550, USA
[4]KIPAC, Stanford University, Stanford, CA 94305-4060, USA
[5]Instituto de Astrofisica, Facultad de Fisica, Pontificia Universidad Catolica de Chile, Av. Vicuna Mackenna 4860, 782-0436 Macul, Santiago, Chile
[6]Physics Department and Columbia Astrophysics Laboratory, Columbia University, 538 West 120th Street, New York, NY, 10027, USA

ABSTRACT

We report on simultaneous *NuSTAR* and *XMM-Newton* observations of the magnetar 1E 1048.1−5937, along with *Rossi X-ray Timing Explorer (RXTE)* data for the same source. The *NuSTAR* data provide a clear detection of this magnetar's persistent emission up to 20 keV. We detect a previously unreported small secondary peak in the average pulse profile in the 7–10 keV band, which grows to an amplitude comparable to that of the main peak in the 10–20 keV band. We show using *RXTE* data that this secondary peak is likely transient. We find that the pulsed fraction increases with energy from a value of ∼0.55 at ∼2 keV to a value of ∼0.75 near 8 keV but shows evidence for decreasing at higher energies. After filtering out multiple bright X-ray bursts during the observation (An et al. 2014), we find that the phase-averaged spectrum from combined *NuSTAR* and *XMM* data is well described by an absorbed double blackbody plus power-law model, with no evidence for the spectral turn-up near ∼10 keV as has been seen in some other magnetars. Our data allow us to rule out a spectral turn-up similar to those seen in magnetars 4U 0142+61 and 1E 2259+586 of $\Delta\Gamma \gtrsim 2$, where $\Delta\Gamma$ is the difference between the soft-band and hard-band photon indexes. The lack of spectral turn-up is consistent with what has been observed from an active subset of magnetars given previously reported trends suggesting the degree of spectral turn-up is correlated with spin-down rate and/or spin-inferred magnetic field.

Keywords: stars: neutron —stars: magnetars — stars: magnetic field — pulsars: general — X-rays: stars—pulsars: individual (1E 1048.1−5937)— X-rays: bursts

1. INTRODUCTION

Magnetars have hard X-ray spectra that represent an interesting puzzle. Previously considered to be 'soft' X-ray sources (e.g. Mereghetti & Stella 1995; van Paradijs et al. 1995), with energy spectra falling rapidly below ∼10 keV owing to a steep ($\Gamma \sim -3$ to -4) power-law photon index, the discovery of hard X-ray emission from several magnetars (Revnivtsev et al. 2004; Kuiper et al. 2004, 2006), and the realization that their spectra can *rise* in energy above 10 keV, clearly demonstrated that in some cases, most of the energy in persistent magnetar emission arises in the hard X-ray band.

With now 8 magnetars exhibiting observable high energy emission (see Olausen & Kaspi 2014, and references therein), some possible trends have been noted. The pulsed fraction of the hard X-ray emission has been suggested to rise with energy to reach ∼100% by ∼100 keV (Kuiper et al. 2006) although more recent studies using the *Nuclear Spectroscopic Telescope Array* (*NuSTAR*) have suggested otherwise for one source (An et al. 2013). The spectra of many magnetars appear to continue rising above ∼100 keV (Kuiper et al. 2006; den Hartog et al. 2008) although evidence for a spectral turnover near 300 keV was detected using *INTEGRAL* in the magnetar 4U 0142+61 (den Hartog et al. 2008). Kaspi & Boydstun (2010) noticed a possible anti-correlation between the degree of the soft–hard spectral turnover and either the frequency derivative or the magnetic field strength (see also Enoto et al. 2010).

The physical origin of magnetar hard X-ray emission is not yet well understood. Several models have been proposed in the literature (Heyl & Hernquist 2005; Baring & Harding 2007; Thompson & Beloborodov 2005; Beloborodov & Thompson 2007) although each has been argued to be problematic (see, e.g. Kaspi & Boydstun 2010, for a discussion). Most recently, Beloborodov (2013) proposed a model that explains the hard X-ray emission as being due to escaping radiation from photons

scattered by relativistic particles in the outer regions of large active magnetic loops called 'j-bundles'. This model has been successfully applied to *NuSTAR* detections of magnetars 1E 1841−045 (An et al. 2015), 1E 2259+586 (Vogel et al. 2014) and 4U 0142+61 (Tendulkar et al. 2015), as well as other observations (Hascoët et al. 2014), yielding interesting constraints on source geometries.

1E 1048.1−5937 is the only persistently bright magnetar (here 'bright' is defined as quiescent 2–10 keV unabsorbed flux $> 5 \times 10^{-12}$ erg cm^{-2} s^{-1}) not yet to have shown clear persistent hard X-ray emission. Though monitored for many years with the *Rossi X-ray Timing Explorer (RXTE)* Proportional Counter Array (PCA) (e.g. Dib et al. 2009; Dib & Kaspi 2014), and in spite of the PCA's excellent sensitivity to hard X-rays albeit with no focusing capability, 1E 1048.1−5937 was not detected in detailed analysis by Kuiper et al. (2006), although Leyder et al. (2008) did report a marginal detection of unpulsed flux (4.5σ) in *INTEGRAL* data in the 22–100 keV band.

NuSTAR observed 1E 1048.1−5937 in 2013 in order to search for persistent hard X-ray emission. In this 320-ks observation, eight bright X-ray bursts were detected fortuitously; these have been reported on by An et al. (2014). Although bursts from this source have been previously detected (e.g. Gavriil et al. 2002; Gavriil & Kaspi 2004; Dib & Kaspi 2014), they are rare (five bursts were detected in 2.9 Ms for an average burst rate of one per week, assuming bursts are produced randomly, consistent with the behavior of this source). Hence the detection of eight bursts in 320 ks was somewhat unexpected, although in many magnetars bursts are seen to be clustered (e.g. Kaspi et al. 2003).

It spite of the bursting behavior, the pulsar's persistent emission during the *NuSTAR* observation is known from independent *Swift* X-ray Telescope monitoring observations (Archibald et al. 2015) to have been nominal.

Here we report on these same 2013 *NuSTAR* observations of 1E 1048.1−5937, this time focusing on the persistent hard X-ray emission. We detect, for the first time, pulsations above ∼10 keV, only the 9th such magnetar detection yet. We show that these pulses are detected as high as 20 keV but no higher, precluding the same dramatic spectral turn-up observed in some other magnetars.[1]

2. INSTRUMENTS AND OBSERVATIONS

In order to study the pulsar's hard X-ray emission, we conducted simultaneous observations using *NuSTAR* and ESA's *X-ray Multi-Mirror Mission* (*XMM-Newton*).

NuSTAR is a NASA Small Explorer (SMEX) satellite mission operating in the 3−79 keV range (Harrison et al. 2013). This is the first hard X-ray satellite mission (above ∼10 keV) with focusing capability. The instrument features two focal plane modules, dubbed FPMA and FPMB. Each module consists of a reflective, multilayer-coated, focusing telescope (Hailey et al. 2010; Craig et al. 2011) with a CdZnTe detector sitting in the focal plane (Harrison et al. 2010). The achievable FWHM energy resolution varies from 400 eV at 10 keV to 900 eV at 68 keV, while the angular resolution of the instrument is characterized by a half-power diameter (HPD) of 58″ and a FWHM of 18″.

The *XMM-Newton* observatory (Jansen et al. 2001) focuses on the soft X-ray regime (0.1 – 10 keV) using its three on-board X-ray telescopes. Each of these Wolter I grazing-incidence optics consists of 58 coaxially and co-focally nested mirrors. A European Photon Imaging Camera (EPIC) sits at the prime focus of each of the three telescopes. Two of these Charge-Coupled Devices (CCDs) make use of the MOS technology (MOS-1/MOS-2), while the third detector is a pn-CCD (Turner et al. 2001; Strüder et al. 2001). The achievable energy resolution lies between 70 – 80 eV and the EPIC point-spread function is 5 – 6″ FWHM (15″ HPD).

NuSTAR observed 1E 1048.1−5937 in July of 2013. A total of four separate observations took place between July 17 and July 27 (*NuSTAR* observation IDs 30001024002, 30001024003, 30001024005 and 30001024007). As mentioned above, in these observations, which together comprised a total of 320-ks of exposure, eight bright X-ray bursts were detected (An et al. 2014). For the analysis presented in this paper we used the same data set, but excluded times of burst activity (bursts and their tails) to avoid contaminating timing and spectral results with burst emission.

The selected portions of the light curve are shown in red in the top panel of Figure 1. Note that only 3 of the 4 *NuSTAR* data sets could be used in this analysis as the fourth was too contaminated by bursts and their tails (see An et al. 2014). The corresponding good time intervals (GTI) used in our analysis lie between MJDs 56490.33 – 56490.93, MJDs 56492.81 – 56496.19 and MJDs 56498.19 – 56499.14. The total exposure time of all GTIs is 210 ks for the presented analysis. Table 1 provides details on all data sets used in this analysis.

XMM-Newton observed 1E 1048.1−5937 from July 22-23, 2013 (Observation ID 0723330101), simultaneous with part of the *NuSTAR* observations, as shown in Figure 1. Our *XMM* observation made use of the EPIC pn-CCD as well as the MOS-type detectors (Turner et al. 2001; Strüder et al. 2001). The total exposure time for the EPIC pn-CCD observations was 48 ks, while the

[1] Note that well after our submission of this paper, we were made aware of the work of Weng & Göğüş (2015) who also analyzed these same data and found similar results.

Table 1. Summary of *NuSTAR*, *XMM-Newton* and *Swift* observations of 1E 1048.1−5937 used in this study.

Observatory	Instrument	Mode	ObsID	Date [MJD][a]	Date [yymmdd][a]	Exposure [ks]
NuSTAR	···	···	30001024002	56490.33	130717	24.7/24.5[b]
NuSTAR	···	···	30001024003	56490.97	130717	24.0/0.0[b]
NuSTAR	···	···	30001024005	56492.83	130719	156.7/140.7[b]
NuSTAR	···	···	30001024007	56498.21	130725	111.3/47.4
XMM	EPIC-pn	Full Frame	0723330101	56495.69	130722	48
XMM	EPIC-MOS1/2	Small Window	0723330101	56495.67	130722	64
RXTE	PCA	Good Xenon	see §3.4	52630–54200	021222–070410	939.5
RXTE	PCA	Good Xenon	see §3.4	54500–56000	080204–120314	1101.0

[a] At the start of data acquisition.

[b] Before/after burst data removed, except for the *RXTE*/PCA data, which contained no bursts.

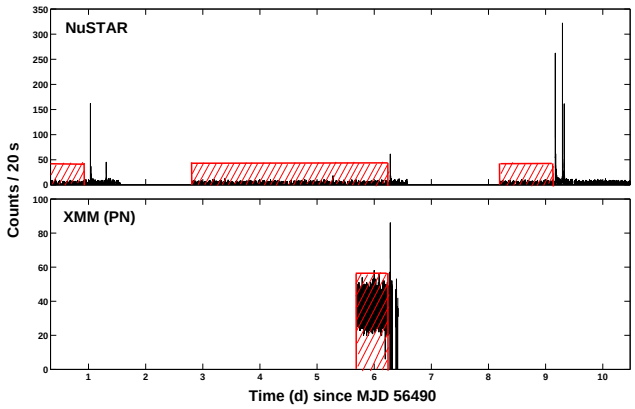

Figure 1. Light curve of *NuSTAR* observation (top) with combined FPMA and FPMB data and *XMM-Newton* observation (bottom) displaying the EPIC-pn data. Red regions indicate good time intervals after excluding the bursts and their tails.

MOS1/2 data set included 64 ks. All cameras were acquiring in imaging mode with the pn-CCD using Full Frame Mode and MOS1/2 detectors running in Small Window Mode.

We processed the *NuSTAR* data using the standard *NuSTAR* Data Analysis Software `NuSTARDAS` version 1.4.1, including the standard data processing routines `nupipeline` and `nuproducts`, with the HEASoft software package[2] (version 6.16) and CALDB[3] (version 20140414). To include the GTIs in our data screening we made use of the `usrgtifile` parameter for the `nupipeline` and `nuproducts` commands. In the subsequent analysis, source events were selected from within a circular region of 60″ radius at the *Chandra* position of 1E 1048.1−5937 (Olausen & Kaspi 2014), while background events were extracted within a circular region of 100″ radius far away from the source. The barycentric correction to the selected events was done using the multi-mission tool command `barycorr` together with the appropriate orbital and clock correction files.

In addition to the phase-averaged spectral analysis described below in §3.2, we conducted a phase-resolved study (§3.3). For this purpose, we defined MJD 56200.00002243577 as the time of phase zero and calculated the phase of each event in both the source and background region using the command `dmtcalc` in the CIAO software package[4] (version 4.6). We then employed the XSELECT tool of the HEASoft package to extract a spectrum in each of the chosen phase ranges. We regrouped the source spectrum to have a minimum of 30 counts per energy bin and conducted all following spectral analyses using XSPEC (version 12.8.2), which is also part of HEASoft. Because there were no significant source counts above 20 keV, we limited our analysis to the energy range of 3 – 20 keV in the *NuSTAR* data. For all our spectral analyses, we assumed interstellar absorption cross sections from Balucinska-Church & McCammon (1992) (with updates from Yan et al. 1998) and abundances from Anders & Grevesse (1989).

To process the *XMM-Newton* data we made use of the `SAS` data analysis software package[5] (version 13.5.0), and employed the most recent calibration files (downloaded July 16, 2014) and standard threads[6] to process the data. In order to avoid pile-up issues we selected an annular region around the source with an inner and outer radius of 3″ and 30″, respectively. The background was selected in a source-free circular region of 60″ in

[2] http://heasarc.nasa.gov/lheasoft/

[3] http://heasarc.gsfc.nasa.gov/docs/heasarc/caldb/caldb_intro.html

[4] http://cxc.harvard.edu/ciao/

[5] http://xmm.esac.esa.int/sas/

[6] http://xmm.esac.esa.int/sas/current/documentation/threads/

radius. The *XMM-Newton* light-curve (Fig. 1, bottom) shows that there was a burst during the *XMM* observation, which was also observed in the *NuSTAR* data as reported by An et al. (2014). For the analysis described in this paper, only the *XMM-Newton* data before the burst were used.

To obtain the phase-resolved spectrum for *XMM-Newton*, we used the `barycen` command to apply the barycenter correction. The phase of each event was then obtained using `phasecalc`. Both commands are part of the standard SAS package. Following these steps we extracted a spectrum for each phase bin with the `evselect` command in the energy range 0.3 – 10 keV and regrouped the data to obtain a minimum of 30 counts per spectral bin.

Because of the bursting seen in the *NuSTAR* data, it is conceivable that tail emission following bursts that may have occured prior to the start of our three data intervals (see Fig. 1) could contaminate the results that follow. Given the short duration of tails seen following 1E 1048.1−5937 bursts (Gavriil et al. 2006; An et al. 2014), even if there had been a bursts prior to all three data intervals, at most 4% of our data would contain tail emission. Nevertheless, we have verified by examining archival data from *Swift*/BAT and *Fermi*/GBM that those instruments detected no bursts from the direction of 1E 1048.1−5937 during the relevant epochs. Additionally, we have verified that there is no evidence for a decreasing count rate at the start of any of the three observing intervals, as would be expected if tails were present there. Given the absence of a decreasing count rate and the properties of the bursts described by An et al. (2014), notably how the spectrum evolves with time, our simulations of the worst-case contamination and find our fitted spectral parameters for the persistent emission could not have been significant affected.

3. ANALYSIS AND RESULTS

3.1. *Timing Analysis*

For the timing analysis, we searched for pulsations in the 3 – 20 keV barycenter-corrected, event list using the H-test (De Jager et al. 1989) and determined the best period for 1E 1048.1−5937 in the *NuSTAR* data to be 6.4616815(3) s. This period is consistent with that found in contemporaenous monitoring observations with the *Swift* X-ray Telescope (Archibald et al. 2015). We folded the barycenter-corrected events with this best-fit period to obtain the pulse profiles in different energy ranges for *NuSTAR* and *XMM-Newton* data separately. The results are shown in Figure 2.

Below 10 keV, the pulse profiles are largely sinusoidal in shape with only one single distinctive peak, in agreement with previous observations (e.g. Tiengo et al. 2005). Interestingly, there is a small secondary peak in the 7–10 keV *NuSTAR* pulse profile, consistent with a small excess apparent in the pulse profile from the *XMM* data in the same energy range, as shown in the bottom left panel of Figure 2. For the first time, pulsations above 10 keV are observed in this source. The secondary peak from the 7–10 keV band grows in amplitude such that the pulse profile of 1E 1048.1−5937 exhibits two peaks in the 10–20 keV energy band. This secondary peak has a harder spectrum than the first and is roughly out of phase by 180°, consistent with being from an opposite pole. However, as described below (§3.4) this secondary peak is not detected in *RXTE* data from past epochs and so appears to be transient. Above about 20 keV, no pulsations were detected, presumably due to a paucity of counts.

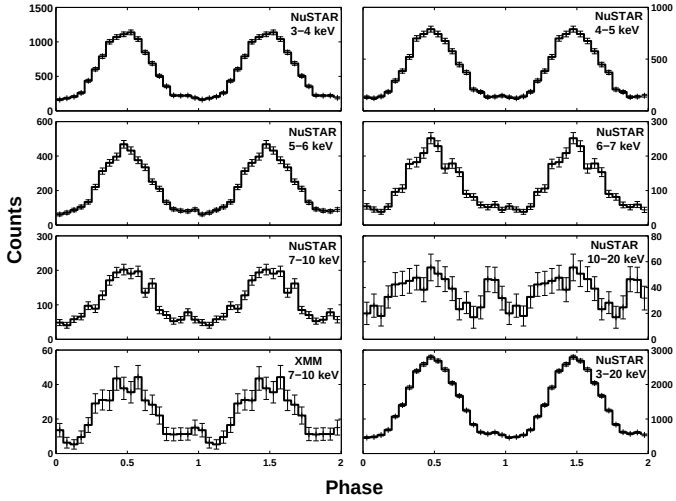

Figure 2. *NuSTAR* pulse profiles in various energy bands after folding with the best-fit period and after excluding the bursts and their respective tails. The full 3–20 keV profile is shown the bottom right plot, and the *XMM* 7–10 keV profile is shown the bottom left plot, for comparison with the *NuSTAR* 7–10 keV plot. Note the secondary peak that appears in this 7–10 keV band, and which grows in relative amplitude in the 10–20 keV band.

We also calculated the pulsed fraction (PF) as a function of energy for our *NuSTAR* and *XMM* observations using the folded pulse profiles and following the prescription described in An et al. (2015). Specifically, we calculated the area pulsed fraction PF_{area} (the difference between pulsed flux and constant flux integrated over a full phase cycle) and the RMS pulsed fraction PF_{RMS} (a measure of the deviation of the pulsed flux from its mean) using 6 harmonics. Note that PF_{area} and PF_{RMS} are expected to differ as they measure different quantities; see An et al. (2015) for details.

Figure 3 shows the results of our pulsed flux analysis for the *NuSTAR* and *XMM* (EPIC-pn) pulse profiles,

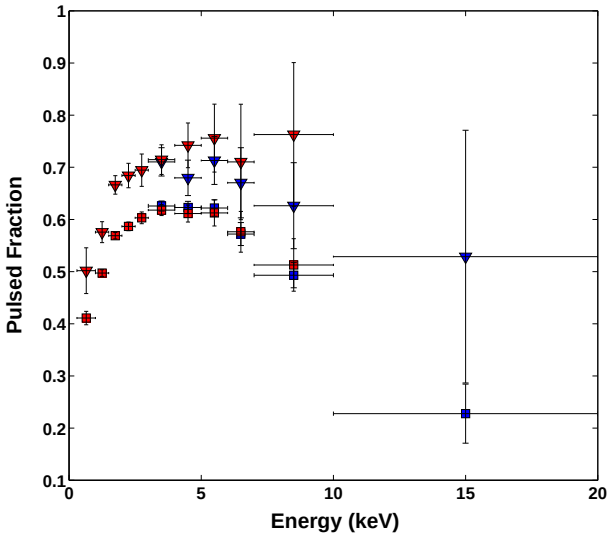

Figure 3. Area (triangles) and RMS (squares) pulsed fractions as a function of energy for the *NuSTAR* and *XMM* (EPIC-pn) pulse profiles. *NuSTAR* data are shown in blue, *XMM* data in red.

specfically PF_{area} and PF_{RMS} as a function of energy. In the Figure, *NuSTAR* data are shown in blue, while red refers to *XMM* (EPIC-pn) data. The area pulsed fractions and the RMS pulsed fractions are displayed as triangles and squares, respectively. The energy bands for the *NuSTAR* data correspond to those shown in Fig. 2, while for the *XMM* data we used the 0.3–10 keV band.

The observed trend for both PF_{area} and PF_{RMS} is a slight increase with energy up to about 5 keV and then a decrease for increasing energies. The latter is not statistically significant for PF_{area} considering the large uncertainties especially in the largest two energy bins, however it is for PF_{RMS}. For energies around 1 keV, PF_{area} is $50\% \pm 4\%$, which rises to about $74\% \pm 4\%$ for energies around 5 keV and "drops" to $53\% \pm 24\%$ for $10-20$ keV. The results for PF_{RMS} are $41\% \pm 1\%$, $61\% \pm 2\%$, and $23\% \pm 6\%$ for energies around 1, 5, and $10-20$ keV, respectively.

3.2. *Phase-Averaged Spectral Analysis*

To study the spectrum of 1E 1048.1−5937, we combined data from *NuSTAR* and *XMM*. The *XMM* data were useful for establishing the low-energy spectrum, particularly the thermal component, since *NuSTAR* is not sensitive below 3 keV. We used only pn *XMM* data for the spectral analysis because of the fewer MOS counts and to minimize cross-calibration systematic errors. For pn we chose only data in the energy interval 0.3–10 keV, and for *NuSTAR* (FPMA+FPMB) only 3–20 keV data were used, because above 20 keV there were insufficient source counts for a meaningful result. We rebinned these data to have a minimum of 30 counts per spectral bin.

We began with a blackbody plus power-law model, often employed for magnetars, and used the `tbabs * const * (cflux * bbody + cflux * powerlaw)` model in XSPEC. We held the pn relative normalization at unity, and let the normalization values of the *NuSTAR* data groups vary. This absorbed blackbody plus power-law model yielded best-fit parameters of absorption $N_H = 1.22 \pm 0.01 \times 10^{22}$ cm^{-2}, blackbody temperature 0.667±0.005 keV, and photon index 3.64±0.02. Our best-fit N_H is significantly higher than that reported by Tam et al. (2008) based on joint fits of *Chandra, Swift* and *XMM* data in the energy range 0.5–7 keV. The different energy ranges and different instruments used may account for the discrepancy; we note that our best-fit N_H is statistically consistent with that measured by Tiengo et al. (2005) (their Observation C) which was based on *XMM* data only, and included data up to 10 keV. We tried different abundance and cross-section models (see §2) but these did not make significant differences to the fit, and resulted in N_H values that differed from the above but at most a few percent. For our best-fit model, the 3–10 keV keV flux in the blackbody component is $(2.03 \pm 0.03) \times 10^{-12}$ erg s^{-1} cm^{-2}, and in the power-law component $(1.78 \pm 0.03) \times 10^{-12}$ erg s^{-1} cm^{-2}. The reduced χ^2 to the fit described above was 1.07 with 1352 degree of freedom which has probability ∼4% of being due to chance. This low probability is suggestive – though not conclusive – that the model is not optimal. Figure 4 (top) shows the spectrum and residuals after subtraction of this simple model; indeed the residuals have some structure that suggests this model is not optimal.

For this reason, we also tried fitting these data with multiple different models. Specifically, we employed an absorbed blackbody plus broken power-law model to search for a spectral break, as is seen in some other magnetars. This model yielded a reduced χ^2 value of 1.03 (see Table 2). Figure 4 (bottom) shows residuals for the broken power-law model. For completeness, we also tried a double blackbody plus power-law model as has been used in other hard X-ray analyses of magnetars (Hascoët et al. 2014), as well as a double blackbody plus broken power-law model, both with absorption. These yielded similar goodness-of-fits as the blackbody plus broken power law. Best-fit spectral parameters for all the models we tried are provided in Table 2. We verified that the improvement of the fits using these models over the simpler 2-component model was statistically significant using simulations. Using `XSPEC`, we created fake datasets having simple blackbody plus power-law spectra with parameters equal to those found when fitting such a model (see above). We then fit these fake data sets with the aforementioned multi-component models (blackbody plus broken power law, double blackbody plus power law, dou-

Table 2. Phase-averaged spectral parameters for joint *NuSTAR* and *XMM* spectral fits.[a]

$Model^b$	N_H (10^{22} cm^{-2})	$kT1$ (keV)	$kT2$ (keV)	Γ_s	E_{break} (keV)	Γ_h	χ^2_{red}/dof
BB+PL	1.22(1)	0.667(5)	···	3.64(2)	···	···	1.07/1352
BB+BknPL	1.14(2)	0.624(8)	···	3.36(5)	6.3(2)	4.4(1)	1.03/1350
2BB+PL	1.17(2)	0.53(3)	0.85(5)	3.67(5)	···	···	1.03/1350
2BB+BknPL	1.22(5)	0.51(2)	0.87(5)	4.1(3)	5.3(8)	3.0(5)	1.03/1348

a Uncertainties are at the 1σ confidence level. *NuSTAR* energy range is 3–20 keV with combined FPMA and FPMB data. *XMM* energy range is 0.3–10 keV with pn data only.
b BB: blackbody, 2BB: two blackbodies, PL: power law, BknPL: broken power law.

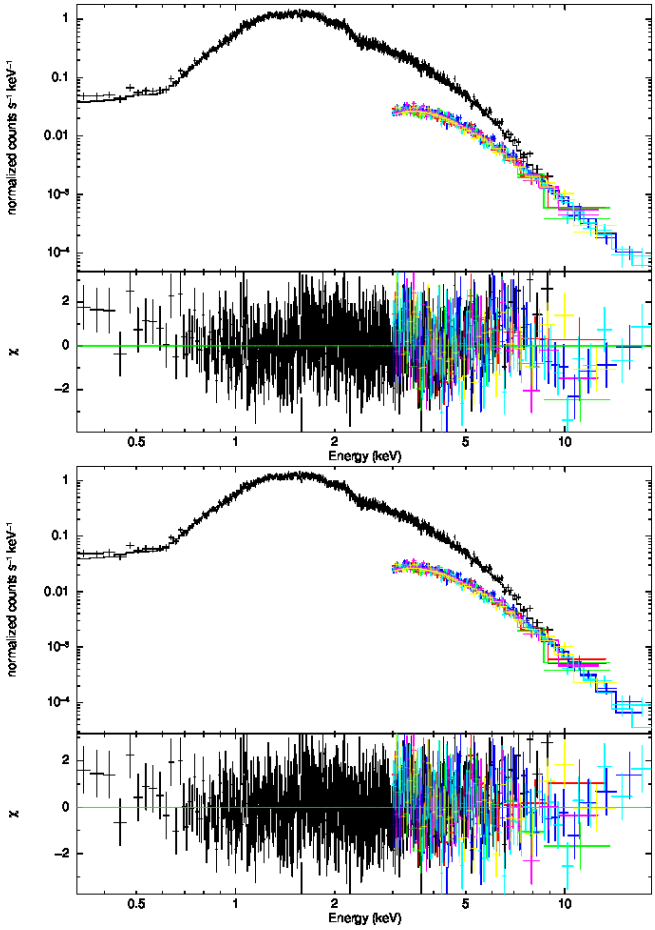

Figure 4. Joint spectral fitting results using *NuSTAR* (multi-colored) and *XMM*/pn (black) data, shown such that each spectral bin has a minimum of 80 counts. We used all the good-time-interval *NuSTAR* data in the range 3–20 keV, and *XMM*/pn data in the range 0.3–10 keV. Top: Fit and residuals for an absorbed blackbody plus power-law model. Bottom: Fit and residuals for a model consisting of an absorbed blackbody plus a broken power law. See Table 2 for fit details.

ble blackbody plus broken power law) and recorded the change in fit statistic. For each trial model, in 1000 trials, in no case did the fit statistic change by an amount even close to that measured for the real data set. We hence conclude with >99.9% confidence that the improvement in fit for the 3-component models is required by the data.

Importantly, for the blackbody plus broken power-law model, the best-fit results in a spectral break at 6.3 keV, and a significant spectral *softening*, with power-law index changing from 3.36 to 4.4. This is quite different from what has been observed for other magnetars for which hard X-ray emission has been detected (see Olausen & Kaspi 2014, for a summary).

To investigate this possible softening further, and because there exists strong covariance between the break energy and change in photon index, we did the following analysis. Noting that a double blackbody plus power law provides a reasonable parameterization of the data, we used the best-fit absorbed double blackbody plus power-law model parameters (see Table 2) and kept them fixed while fitting an absorbed double blackbody plus broken power-law model. We then held the spectral break fixed at values between 3 and 15 keV, at 1 keV intervals, each time fitting only for the hard-band photon index, Γ_h. The results are shown in Figure 5. The Γ_h fit in this way shows marginal evidence for spectral hardening, rather than softening, however it is not statistically significant. We use this analysis instead to estimate an upper limit on any spectral change. Assuming a fiducial break energy of 10 keV, we set a 3σ limit on Γ_h to be >1.8, which limits any change in the power-law index from the soft band to be $\Gamma_s - \Gamma_h = 3.67 - 1.8 \equiv \Delta\Gamma < 1.9$.

We performed additional simulations to investigate this result and in particular ask the question of whether we can rule out spectral turn-ups as have been seen in other magnetars. We took from the literature summarized by Kaspi & Boydstun (2010) the spectra of magnetars 4U 0142+61, 1E 1841−045, 1E 2259+586 and 1RXS J1708−4009, specifically their respective spectral break energies and degree of spectral turn-up, as parameterized by $\Delta\Gamma$. On top of our best-fit absorbed double blackbody plus power-law model, we added a spectral break and generated fake spectra in XSPEC using the `fakeit` command. The fake spectra were grouped to have at least 20 counts per spectral bin. Spectral fits were then performed in the 3–79 keV band with double blackbody plus broken power-law and a double blackbody plus power-law models, and the F-test probability was calculated given the results of every fit. The F-test probabilities (useful since we are comparing nested

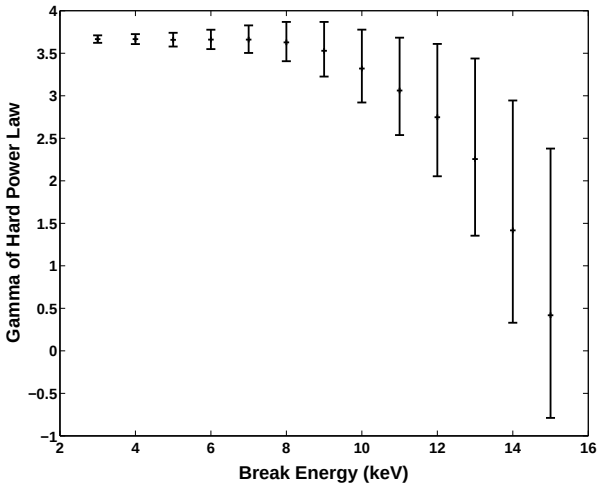

Figure 5. Best-fit hard-band photon index Γ_h as a function of assumed break energy. In making this plot, we held fixed the best-fit parameters from the absorbed double blackbody plus power-law model (see Table 2) in an absorbed double blackbody plus broken power-law model; we held the break energy at integer values in keV ranging from 3 to 15 keV, each time fitting for Γ_h using the *XMM* and *NuSTAR* data jointly.

models) suggested that we can rule out with confidence $\Gamma_s - \Gamma_h < 1.9$. This is consistent with our independent analysis above, which gives us confidence we have found a robust limit.

In particular, we rule out spectral turn-ups like those observed in 4U 0142+61 (E_b = 12 keV, $\Delta\Gamma$ = 3.6) and 1E 2259+586 (E_b = 11.5 keV, $\Delta\Gamma$ = 2.9) with very high confidence (probability 9×10^{-25} and 2×10^{-15}, respectively), that for 1RXS J1708−4009 (E_b = 16 keV, $\Delta\Gamma$ = 1.9) at the 95% confidence level, but cannot rule out that for 1E 1841−045 (E_b = 13.5 keV, $\Delta\Gamma$ = 0.7) with any confidence (probability 0.14). We thus conclude that we can rule out $\Delta\Gamma \gtrsim 2$ for 1E 1048.1−5937.

3.2.1. *Upper Limit on 20–79 keV Flux*

In addition, we calculated the 3σ upper limit on the total, phase-averaged flux for 1E 1048.1−5937 in the 20 – 79 keV range using the conservative approach of Pivovaroff et al. (2000) to determine the count rate upper limit. This yielded an upper limit of $7.7(3) \times 10^{-3}$ cts s^{-1}. We then used the NASA HEASARC tool WebPIMMs[7] based on PIMMS version 4.8 to obtain an estimate on the flux upper limit by using the values for hydrogen column density N_H and the photon index of the expected power law[8] (PL). This yielded $3.3(1) \times 10^{-12}$ ergs cm^{-2} s^{-1} using

[7] https://heasarc.gsfc.nasa.gov/cgi-bin/Tools/w3pimms/w3pimms.pl

[8] We neglected the blackbody contribution to the energy range from 20 – 79 keV

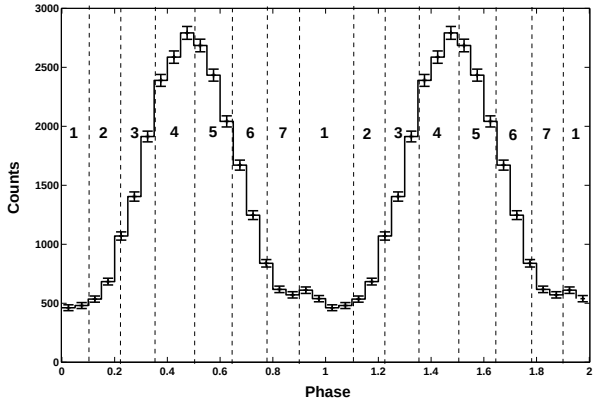

Figure 6. The 3–20 keV pulse profile of our *NuSTAR* observation. For phase-resolved spectroscopy, the pulse profile was divided into seven parts, shown using black vertical dashed lines. Phase 1 is 0.0–0.1 and 0.9–1.0, phase 2 is 0.1–0.225, phase 3 is 0.225–0.35, phase 4 is 0.35–0.5, phase 5 is 0.5–0.65, phase 6 is 0.65–0.775, and phase 7 is 0.775–0.9.

the McGill Online Magnetar Catalogue[9] ($N_H = 0.97(1) \times 10^{22}$ cm^{-2}, $\Gamma = 3.14(11)$) and $2.9(1) \times 10^{-12}$ ergs cm^{-2} s^{-1} for the best-fit values determined in our spectral analysis (see Table 2), i.e. $N_H = 1.22(1) \times 10^{22}$ cm^{-2}, $\Gamma = 3.64(2)$. To obtain a more robust upper limit on the 20 – 79 keV we then used the `fakeit` command in XSPEC taking into account the *NuSTAR* response, which yields the 3σ flux upper limit of $4.15(13) \times 10^{-12}$ ergs cm^{-2} s^{-1} (20 – 79 keV) for our best-fit values (Table 2).

3.3. *Phase-Resolved Spectral Analysis*

We defined MJD 56200.00002243577 as phase zero and used the period provided by the H-test (see §3.1) to obtain folded light curves for the *NuSTAR* and *XMM* data in the 3–20 keV and 0.3–10 keV bands, respectively. We divided the folded light curves into seven parts, as shown in Figure 6, echoing the phases defined by Tiengo et al. (2005). We adopted an absorbed blackbody plus power-law model to fit each phase bin. The best-fit absorption, N_H, 1.22×10^{22} cm^{-2}, from the phase-averaged fitting (see §3.2), was used and held fixed in the phase-resolved spectral analysis. The simple absorbed blackbody plus power-law model fit all phase bins well. The results are summarized in Figure 7, where we show the variability of the model parameters with pulse phase. The blackbody temperature in this spectral parameterization is varying significantly; a χ^2 test yields a 0.2% probability of the observed variation being due to chance. The blackbody temperature is minimal at pulse maximum, suggesting spectral hardening away from the main pulse. On the other hand, in our data, the variation of the power-law index suggests the main pulse is harder

[9] http://www.physics.mcgill.ca/ pulsar/magnetar/main.html

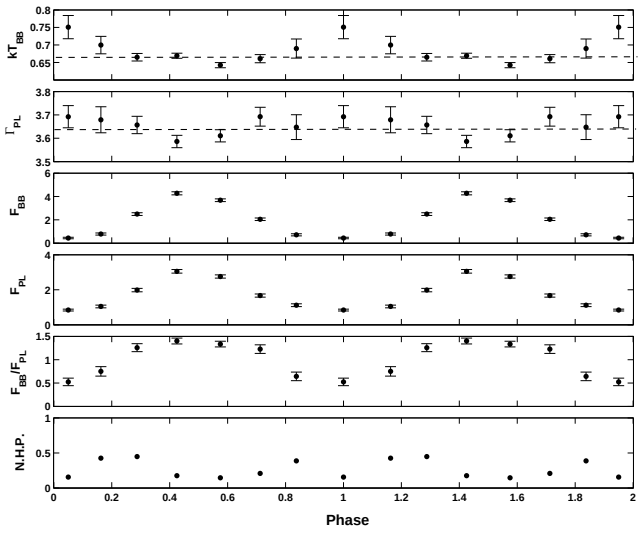

Figure 7. Phase-resolved spectral parameters determined assuming an absorbed blackbody plus power-law model. From top to bottom: the blackbody temperature in units of keV, the power-law index, 3–10 keV unabsorbed flux of the blackbody component in units of 10^{-12} erg s^{-1} cm^{-2}, 3–10 keV unabsorbed flux of the power-law component in units of 10^{-12} erg s^{-1} cm^{-2}, the ratio of the blackbody flux to the power-law flux in the 3–10 keV band, and the probability of obtaining the best-fit reduced χ^2 for the spectral fit. The error bars indicate 1σ uncertainty ranges. Dashed lines represent best-fit phase-averaged values (see Table 2).

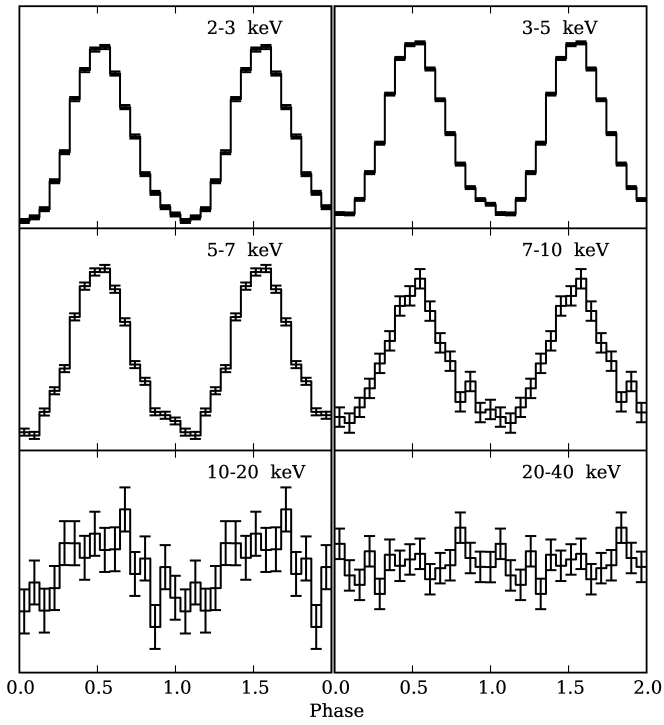

Figure 8. *RXTE*/PCA pulse profiles for 1E 1048.1−5937 in various energy bands. Note the absence of a secondary peak in the 10–20 keV band, in contrast to that observed with *NuSTAR* (Fig. 2). Also note the absence of any pulsations in the 20–40 keV band.

than the off-pulse contribution, however a χ^2 test indicates the variation is not significant, with a 17% chance of the variation being due to chance. Our analysis finds that the ratio of thermal to non-thermal flux is a maximum at the pulse peak. We note that the secondary peak we observe in the 10–20 keV band suggests spectral hardening away from the main peak, however at a level that is small and hence difficult to quantify.

3.4. *Long-term RXTE Observations of 1E 1048.1−5397*

In order to confirm the absence of a spectral turn-up in 1E 1048.1−5937 observed by *NuSTAR*, as well as to investigate the secondary peak we detected in the 10–20 keV *NuSTAR* pulse profile, we analyzed observations of 1E 1048.1−5937 from the Proportional Counting Array (PCA) aboard *RXTE*. The PCA consists of five collimated xenon/methane multianode proportional Counter Units (PCUs) which are sensitive to photons in the 2–60 keV range (Jahoda et al. 1996; Jahoda et al. 2006). 1E 1048.1−5937 was monitored with the PCA regularly for most of the lifetime of *RXTE*; see Dib & Kaspi (2014) for a summary. For all observations of 1E 1048.1−5937, the PCA was operated in "Good Xenon" mode, which provides 1-μs resolution for photon arrival times. These observations were obtained from the HEASARC archive and reduced to the barycenter using the `barycorr` tool in HEASoft version 6.16. Observations were filtered to remove non-astrophysical events using `xtefilt`.

As 1E 1048.1−5937 has experienced several long-term flux flares (see Dib & Kaspi 2014; Dib et al. 2009; Gavriil & Kaspi 2004), we selected only observations from MJDs 52630–54200 and from MJDs 54500–56000, two periods of time where the reported 2–20 keV flux was relatively stable. This resulted in 2.06 Ms of data with an average of 2.07 PCUs on. Observations were folded using local ephemerides from Dib & Kaspi (2014), and then aligned by cross-correlating the profiles in the 2.0–5.5 keV band, where the signal-to-noise ratio is highest in these data.

In this data set, a pulsed signal is detectable at the lower-energy end of the PCA band and into the 10–20 keV band. PCA pulse profiles for various energy bands, including 10–20 keV, are shown in Figure 8. Note the absence of any evidence of a secondary peak in the 10–20 keV PCA profile, in contrast to that seen in the *NuSTAR* data (see Fig. 2). This is also consistent with what was reported by Kuiper et al. (2006). This demonstrates that this profile feature is likely transient in nature. Also note the apparent absence of any pulsations in the 20–40 keV PCA band. There is a possible hint of a secondary feature in the 7–10 keV band, however it is not statistically significant.

We present pulsed count rates for the different en-

Table 3. *RXTE*/PCA Pulsed Fluxes for 1E 1048.1−5937

Band	Pulsed Count Rate (Counts PCU^{-1}s^{-1})	Unabsorbed Pulsed Flux[a] (erg cm^{-2} s^{-1})
2–3 keV	0.0813 ± 0.0005	$(4.84 \pm 0.03) \times 10^{-12}$
3–5 keV	0.150 ± 0.001	$(1.48 \pm 0.01) \times 10^{-12}$
5–7 keV	0.060 ± 0.001	$(5.38 \pm 0.09) \times 10^{-13}$
7–10 keV	0.017 ± 0.001	$(1.7 \pm 0.1) \times 10^{-13}$
10–20 keV	0.005 ± 0.001	$(0.2 \pm 0.25) \times 10^{-13}$
20–40 keV	$0. \pm 0.002$	$< 2 \times 10^{-13}$

a Pulsed flux calculated using WebPIMMs assuming an absorbed power-law
plus blackbody with $N_H = 1.22 \times 10^{22}$cm^{-2}, $\Gamma = 3.64$, and $kT = 0.667$.

ergy bands in Table 3. To convert the *PCA* pulsed count rate into unabsorbed pulsed fluxes, we used WebPIMMs, assuming the phase-averaged spectral parameters we found in §3.2. These PCA count rates are consistent within uncertainties with the results from our *XMM*/*NuSTAR* analysis.

4. DISCUSSION & CONCLUSIONS

Our joint *NuSTAR* and *XMM* data have provided a clear detection of pulsed emission from 1E 1048.1−5937 up to 20 keV. We have discovered a previously unreported small secondary peak in the average pulse profile in the 7–10 keV band, which grows to an amplitude comparable to that of the main peak in the 10–20 keV band. *RXTE*/PCA data averaged over several years prior to these new observations do not show any evidence of the secondary peak, indicating it is transient. We also have shown that the pulsed fraction of 1E 1048.1−5937 increases with energy from ∼2 keV to a value of ∼0.75 near 8 keV but shows evidence for decreasing at higher energies. In our spectral analysis, after filtering out multiple bright X-ray bursts (An et al. 2014), we have shown that the source's phase-averaged spectrum is well described (though not uniquely) by an absorbed double blackbody plus power-law model. The data show no evidence for the spectral turn-up near ∼10 keV seen in some other magnetars. Indeed, for 1E 10481.1−5937, we can rule out a spectral turn-up similar to those seen in magnetars 4U 0142+61 and 1E 2259+586 of $\Delta\Gamma \gtrsim 2$. We have also studied the phase-resolved spectrum and have observed clear spectral changes with rotational phase.

It is important to compare the *NuSTAR*-constrained hard X-ray flux of 1E 1048.1−5937 with other estimates, in order to look for variability. The marginal *INTEGRAL* detection of 1E 1048.1−5937 (Leyder et al. 2008) in the 22–100 keV band was reported without any spectral information, but with a count rate. By comparing the count rate with that reported for a different source (η Carina) in the same paper, and assuming the two sources have similar spectra in that energy band, we infer a 22–100 keV flux of $\sim 5 \times 10^{-12}$ erg s^{-1} cm^{-2}. This is nominally just above our 3σ upper limit in the 20–79 keV band (see §3.2.1). However given the uncertainties particularly in the *INTEGRAL* value, the two fluxes cannot be considered inconsistent. Nevertheless we may ask, given the soft X-ray variability seen in the source (Dib & Kaspi 2014; Archibald et al. 2015), whether the *INTEGRAL* or *NuSTAR*/*XMM* data were taken at substantially different phases in the source's X-ray flux evolution. If so, the comparison of their hard X-ray fluxes, however crude, may not make sense. The *INTEGRAL* data were averaged over several years, mostly from May 2003 to June 2005. During that time span, the 2–10 keV flux of 1E 1048.1−5937 was slowly declining following a bright flare in mid-2002 and the source was undergoing rapid (yet unexplained) torque variations during the first half of the interval (Gavriil & Kaspi 2004; Dib & Kaspi 2014). On the other hand, the *NuSTAR*/*XMM* data were also taken during the decline of the source flux following a flux flare at the start of 2012, but after the cessations of the strong torque variability following that event (Archibald et al. 2015). Hence the source did exhibit somewhat different rotational behavior during the reported *INTEGRAL* observing epoch and that of our observations, although this, and the uncertainty in the *INTEGRAL* flux, are insufficient for concluding the hard X-ray flux varies. The consistency of the pulsed fluxes from *RXTE*/PCA (Table 3) with those from our *NuSTAR*/*XMM* analysis strengthen our conclusion that we find no evidence for flux variation in the hard band for this source, although this is not a strong conclusion.

The absence of an observed spectral turn-up is interesting and not unexpected in the model of Beloborodov (2013). One possible explanation is unfavourable geometry. If the object is viewed close to the rotation axis, e.g. at 10°–20°, and the magnetic dipole axis is weakly inclined to the spin axis (as suggested by observations; see Hascoët et al. 2014), then the line-of-sight to the emission remains close to the magnetic axis at all rotation phases. In this case the predicted hard X-ray component is generally weak (see Fig. 7 in Beloborodov 2013). In other words, the source may actually produce copious hard X-rays, but we do not observe them due to an unfavourable viewing angle. The geometry of an axisymmetric j-bundle viewed near the magnetic axis may also be consistent with the reduction of pulsed fraction at high energies (Fig. 3). On the other hand, for a small angle between the line-of-sight and the rotation axis, a high pulsed fraction at low energies as is observed would not obviously be expected. It could be that the inclination is larger but we do not see the j-bundle because it is not axisymmetric and instead confined to a small range

of magnetic azimuth, so that its field lines are never tangent to our line of sight (and therefore do not emit hard X-rays toward our direction). Another possibility is that the object has a weak or non-existing magnetic twist/j-bundle. However, in this case it is unclear why its emission extends to 20 keV.

The absence of an observed spectral turn-up is consistent with a trend noted by Kaspi & Boydstun (2010) between degree of spectral upturn and both spin-inferred magnetic field strength and spin-down rate in magnetars. The spin-inferred surface dipolar magnetic field strength of 1E 1048.1−5937 is $\sim 4 \times 10^{14}$ G, but because its spin-down rate can vary by over a factor of 10 (Archibald et al. 2015), B inferred from this spin-down should be regarded with caution. The trends noted by Kaspi & Boydstun (2010) suggested that 1E 1048.1−5937 should have a hard-band Γ_h of 1–2, and that the difference between soft-band and hard-band photon indexes, $\Gamma_s - \Gamma_h \equiv \Delta\Gamma$, should be 0–1.[10] From the current data, we cannot constrain Γ_h very strongly. However we can rule out sharp spectral upturns as observed in magnetars 4U 0142+61 and 1E 2259+586. In this sense, our results for 1E 1048.1−5937 are consistent with the reported $\Gamma_s - \Gamma_h$ correlation.

The small secondary peak in the pulse profile seen in the 10–20 keV band appears to be a new feature, as previous *RXTE* data (see Fig. 8 and Kaspi et al. 2001; Kuiper et al. 2006) show no evidence for it. This may suggest that the source was not in a true quiescent state during the *NuSTAR*/*XMM* observations, as other temporary features in the pulse profile have been reported, notably near the epochs of bright flux flares (see Dib & Kaspi 2014, and references therein). Indeed the bursting behavior we detected during our observation is consistent with the source being in some form of outburst. On the other hand, at the epoch of our *NuSTAR* and *XMM* data, as discussed above, the source had largely recovered from its 2012 flux flare and was in a relatively rotationally stable phase (Archibald et al. 2015). In any case, the hard-band pulse profile, in contrast to the source hard-band flux, is clearly variable.

In our phase-resolved analysis, we found that the blackbody temperature, as judged from the absorbed blackbody plus power-law model, was highest off-pulse. This is *opposite* to the trend reported by Tiengo et al. (2005), who found the main pulse to have a higher blackbody temperature. We note that the behavior in phase of the power-law index in our analysis, namely a harder Γ on-pulse, is consistent with that seen by Tiengo et al. (2005), however not to the same degree: our power-law index varies by ∼0.1 over a period, while theirs did by ∼0.4. However, an important caveat in this comparison is that in the Tiengo et al. (2005) analysis, no attempt was made to vary the blackbody and power-law components simultaneously, presumably due to lack of counts. Hence, the comparison of the behaviors of either kT or Γ is not exact. Regardless, both analyses find that the ratio of thermal to non-thermal flux is a maximum at the pulse peak, with variation by a factor of ∼3 over the period, although again, Tiengo et al. (2005) do not vary both model components, so the comparison is not ideal.

Our observations have served to continue to flesh out the hard X-ray emission properties of magnetars as a population. For the target in question, 1E 1048.1−5937, the source's faintness at hard X-ray energies precludes detailed modelling using the framework of Hascoët et al. (2014) as has been used in other *NuSTAR* magnetar studies. However, a comparably long second joint *NuSTAR*/*XMM* observation could at least test whether the bursting fortuitously detected in the first observation impacted the hard-band properties, particularly the appearance of the secondary pulse peak. An observation much longer than ours would be required to enable detailed physical modelling. Long-term monitoring with the LAXPC instrument aboard the *Astrosat* mission has the potential to reveal more about the hard X-ray emission of 1E 1048.1−5397, but this will require several megaseconds of exposure. Of the persistently X-ray bright magnetars, 1E 1048.1−5937 is the faintest in the soft band; our faint 10–20 keV detection, in spite of the lengthy *NuSTAR* exposure, demonstrates that *NuSTAR* hard-band detections of fainter magnetars – unless they are in outburst – will be challenging.

We thank Daniel Stern for helpful comments. This work was supported under NASA Contract No. NNG08FD60C, and made use of data from the *NuSTAR* mission, a project led by the California Institute of Technology, managed by the Jet Propulsion Laboratory, and funded by the National Aeronautics and Space Administration. We thank the *NuSTAR* Operations, Software and Calibration teams for support with the execution and analysis of these observations. This research has made use of the *NuSTAR* Data Analysis Software (NuSTARDAS) jointly developed by the ASI Science Data Center (ASDC, Italy) and the California Institute of Technology (USA). Part of this work was performed under the auspices of the U.S. Department of Energy by Lawrence Livermore National Laboratory under Contract DE-AC52-07NA27344. RFA receives support from an NSERC Alexander Graham Bell Canada Graduate Scholarship. JAK was supported by supported

[10] Note, in the text of Kaspi & Boydstun (2010) the authors predicted $\Gamma_h \sim 0-1$, which is not consistent with their own trends. We believe this was an oversight.

by NASA contract NAS5-00136. VMK receives support from an NSERC Discovery Grant and Accelerator Supplement, from the Centre de Recherche en Astrophysique du Québec, an R. Howard Webster Foundation Fellowship from the Canadian Institute for Advanced Study, the Canada Research Chairs Program and the Lorne Trottier Chair in Astrophysics and Cosmology. AMB was supported by NASA grants NNX-10-AI72G and NNX-13-AI34G.

REFERENCES

An, H., Hascoët, R., Kaspi, V. M., et al. 2013, ApJ, 779, 163
An, H., Kaspi, V. M., Beloborodov, A. M., et al. 2014, ApJ, 790, 60
An, H., Archibald, R. F., Hascoët, R., et al. 2015, ApJ, 807, 93
Anders, E., & Grevesse, N. 1989, GeoCoA, 53, 197
Archibald, R. F., Kaspi, V. M., Ng, C.-Y., et al. 2015, ApJ, 800, 33
Balucinska-Church, M., & McCammon, D. 1992, ApJ, 400, 699
Baring, M. G., & Harding, A. K. 2007, Ap&SS, 308, 109
Beloborodov, A. M. 2013, ApJ, 762, 13
Beloborodov, A. M., & Thompson, C. 2007, ApJ, 657, 967
Craig, W. W., An, H., Blaedel, K. L., et al. 2011, in Society of Photo-Optical Instrumentation Engineers (SPIE) Conference Series, Vol. 8147, Society of Photo-Optical Instrumentation Engineers (SPIE) Conference Series, 0
De Jager, O. C., Swanepoel, J. W. H., & Raubenheimer, B. C. 1989, A&A, 221, 180
den Hartog, P. R., Kuiper, L., & Hermsen, W. 2008, A&A, 489, 263
den Hartog, P. R., Kuiper, L., & Hermsen, W. 2008, A&A, 489, 263
Dib, R., & Kaspi, V. M. 2014, ApJ, 784, 37
Dib, R., Kaspi, V. M., & Gavriil, F. P. 2009, ApJ, 702, 614
Enoto, T., Nakazawa, K., Makishima, K., et al. 2010, ApJL, 722, L162
Gavriil, F. P., & Kaspi, V. M. 2004, ApJ, 609, L67
Gavriil, F. P., Kaspi, V. M., & Woods, P. M. 2002, Nature, 419, 142
Gavriil, F. P., Kaspi, V. M., & Woods, P. M. 2006, ApJ, 641, 418
Hailey, C. J., An, H., Blaedel, K. L., et al. 2010, in Society of Photo-Optical Instrumentation Engineers (SPIE) Conference Series, Vol. 7732, Society of Photo-Optical Instrumentation Engineers (SPIE) Conference Series
Harrison, F. A., Cook, W. R., Hiyasaka, H., & McLean, R. 2010, in Semiconductor radiation detection systems, ed. K. Iniewski (Boca Raton, FL: CRC Press)
Harrison, F. A., Craig, W. W., Christensen, F. E., et al. 2013, ApJ, 770, 103
Hascoët, R., Beloborodov, A. M., & den Hartog, P. R. 2014, ApJL, 786, L1
Heyl, J. S., & Hernquist, L. 2005, ApJ, 618, 463
Jahoda, K., Markwardt, C. B., Radeva, Y., et al. 2006, ApJS, 163, 401
Jahoda, K., Swank, J. H., Giles, A. B., et al. 1996, Proc. SPIE, 2808, 59
Jansen, F., Lumb, D., Altieri, B., et al. 2001, A&A, 365, L1
Kaspi, V. M., & Boydstun, K. 2010, ApJL, 710, L115
Kaspi, V. M., Gavriil, F. P., Chakrabarty, D., Lackey, J. R., & Muno, M. P. 2001, ApJ, 558, 253
Kaspi, V. M., Gavriil, F. P., Woods, P. M., et al. 2003, ApJ, 588, L93
Kuiper, L., Hermsen, W., & Mendez, M. 2004, ApJ, 613, 1173
Kuiper, L., Hermsen, W., den Hartog, P. R., & Collmar, W. 2006, ApJ, 645, 556
Leyder, J.-C., Walter, R., & Rauw, G. 2008, A&A, 477, L29
Mereghetti, S., & Stella, L. 1995, ApJ, 442, L17
Olausen, S. A., & Kaspi, V. M. 2014, ApJS, 212, 6
Pivovaroff, M., Kaspi, V. M., & Camilo, F. 2000, ApJ, 535, 379
Revnivtsev, M. G., Sunyaev, R. A., Varshalovich, D. A., et al. 2004, Astronomy Letters, 30, 382
Strüder, L., Briel, U., Dennerl, K., et al. 2001, A&A, 365, L18
Tam, C. R., Gavriil, F. P., Dib, R., et al. 2008, ApJ, 677, 503
Tendulkar, S. P., Hascöet, R., Yang, C., et al. 2015, ApJ, 808, 32
Thompson, C., & Beloborodov, A. M. 2005, ApJ, 634, 565
Tiengo, A., Mereghetti, S., Turolla, R., et al. 2005, A&A, 437, 997
Turner, M. J. L., Abbey, A., Arnaud, M., et al. 2001, A&A, 365, L27
van Paradijs, J., Taam, R. E., & van den Heuvel, E. P. J. 1995, A&A, 299, L41
Vogel, J. K., Hascoët, R., Kaspi, V. M., et al. 2014, ApJ, 789, 75
Weng, S.-S. & Göğüş, E. 2015, ApJ, 815, 15
Yan, M., Sadeghpour, H. R., & Dalgarno, A. 1998, ApJ, 496, 1044

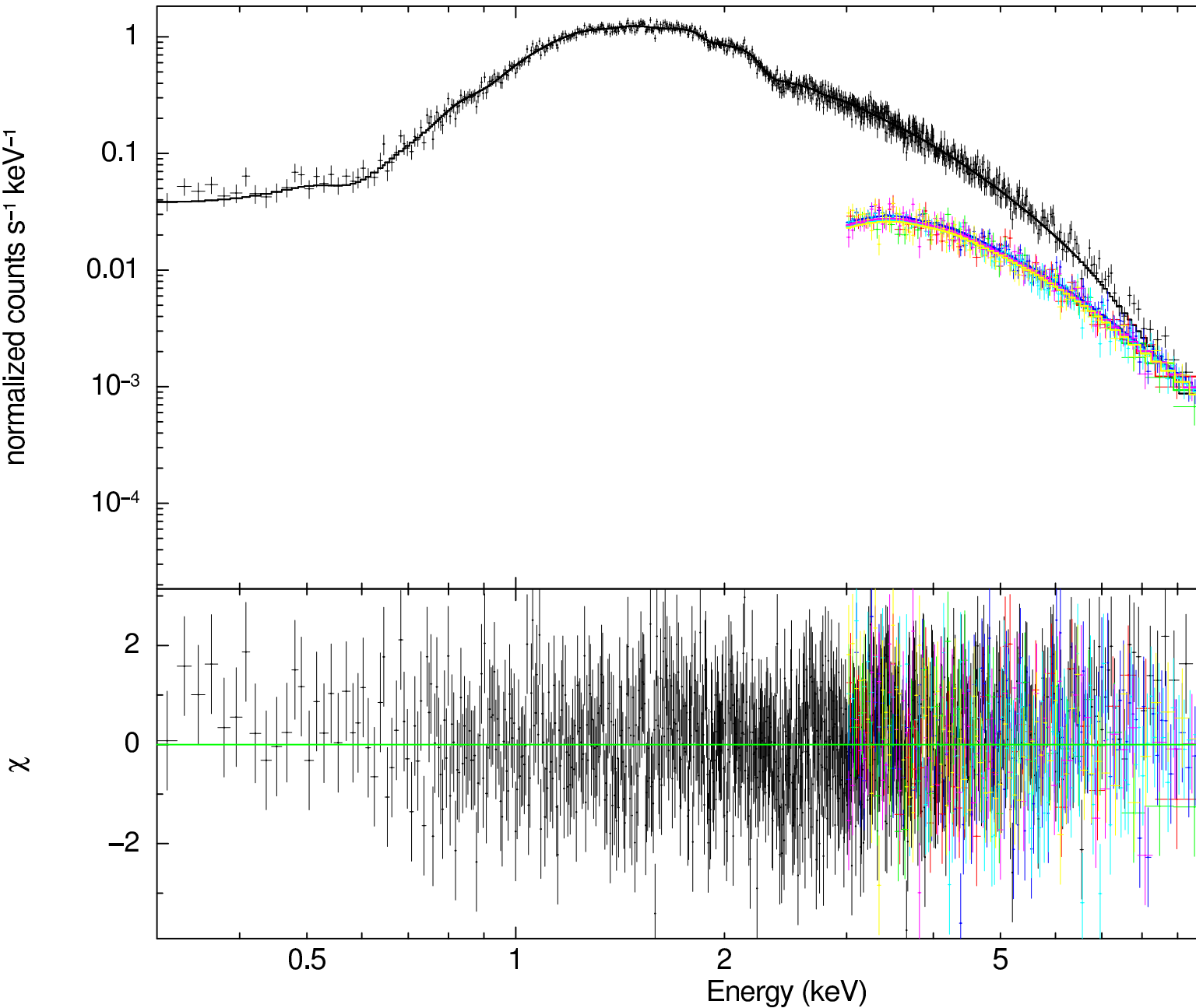
normalized counts s^{-1} keV^{-1}
1
0.1
0.01
10^{-3}
10^{-4}
χ
2
0
−2
0.5
1
2
5
Energy (keV)

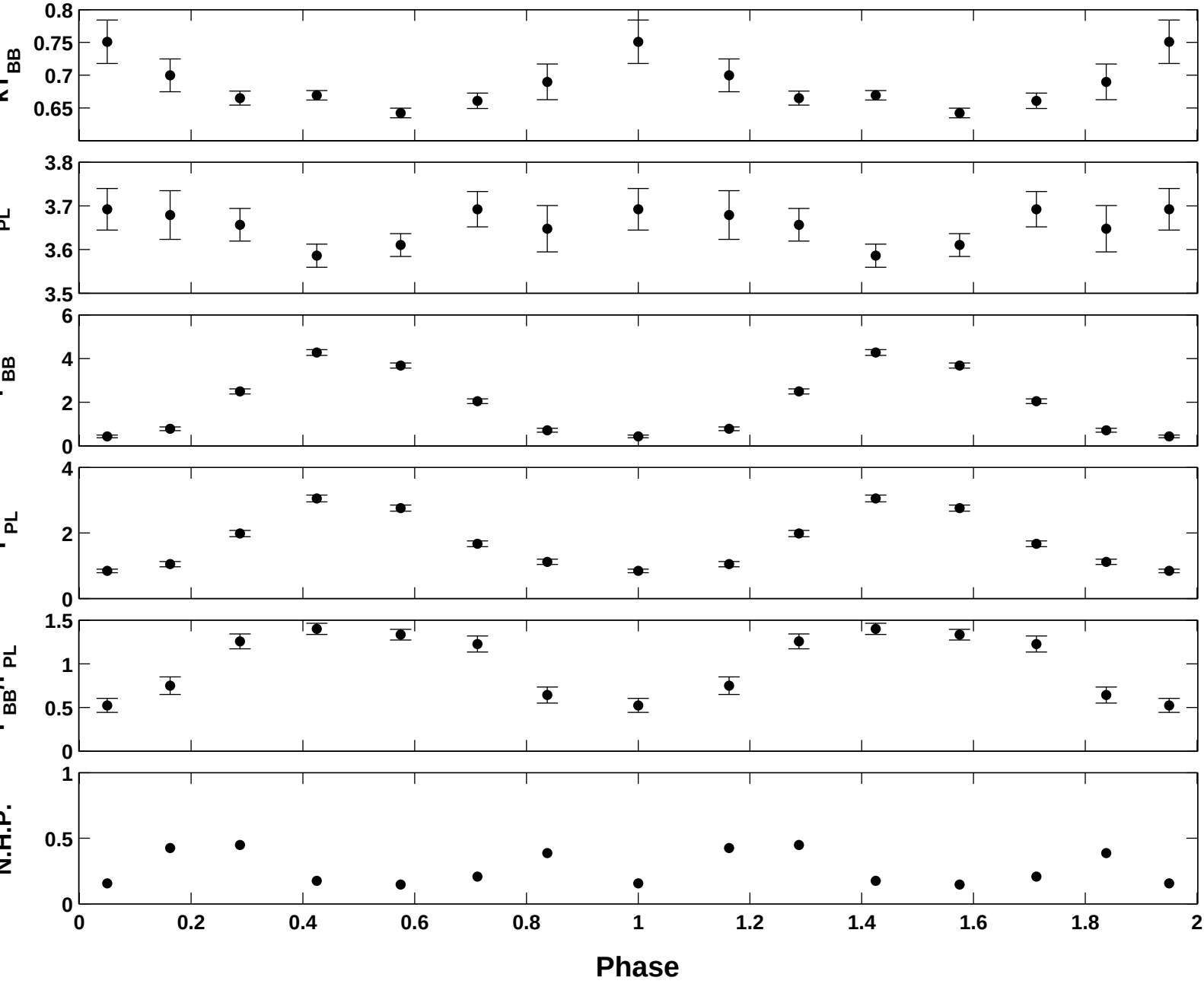
0.8
0.75
0.7
0.65
3.8
3.7
3.6
3.5
6
4
2
0
4
2
0
1.5
1
0.5
0
1
0.5
0
0
0.2
0.4
0.6
0.8
1
1.2
1.4
1.6
1.8
2
Phase

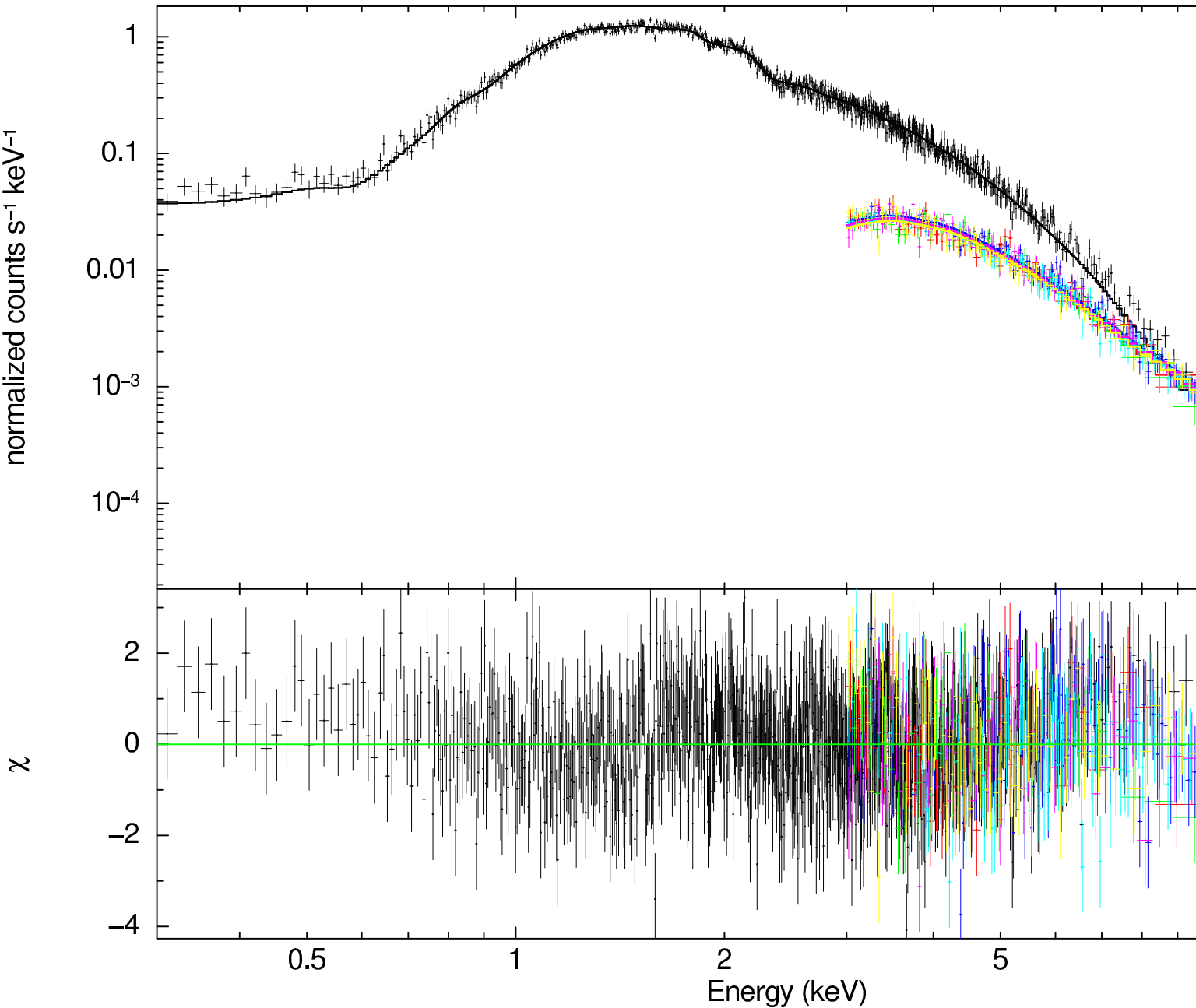
normalized counts s⁻¹ keV⁻¹
1
0.1
0.01
10⁻³
10⁻⁴
χ
2
0
−2
−4
0.5
1
2
5
Energy (keV)